



Cite this: *Soft Matter*, 2020,  
16, 9683

## Free-energy landscape of polymer-crystal polymorphism<sup>†</sup>

Chan Liu,<sup>a</sup> Jan Gerit Brandenburg,<sup>bc</sup> Omar Valsson,<sup>bc</sup> Kurt Kremer<sup>a</sup> and Tristan Bereau<sup>bc\*</sup>

Polymorphism rationalizes how processing can control the final structure of a material. The rugged free-energy landscape and exceedingly slow kinetics in the solid state have so far hampered computational investigations. We report for the first time the free-energy landscape of a polymorphic crystalline polymer, syndiotactic polystyrene. Coarse-grained metadynamics simulations allow us to efficiently sample the landscape at large. The free-energy difference between the two main polymorphs,  $\alpha$  and  $\beta$ , is further investigated by quantum-chemical calculations. The results of the two methods are in line with experimental observations: they predict  $\beta$  as the more stable polymorph under standard conditions. Critically, the free-energy landscape suggests how the  $\alpha$  polymorph may lead to experimentally observed kinetic traps. The combination of multiscale modeling, enhanced sampling, and quantum-chemical calculations offers an appealing strategy to uncover complex free-energy landscapes with polymorphic behavior.

Received 23rd July 2020,  
Accepted 2nd September 2020  
DOI: 10.1039/d0sm01342k  
[rsc.li/soft-matter-journal](http://rsc.li/soft-matter-journal)

### I. Introduction

The complex interplay of molecular interactions can lead to a material exhibiting multiple distinct forms in its solid state.<sup>1</sup> This polymorphism often results in wildly different material properties, making the study of polymorphism both essential for quality control in manufacture, and also a fascinating structure–property problem. Beyond structure and property, the intermediate processing of a material has a key impact on the resulting polymorph. Fundamentally, this stems from two ingredients: (i) the underlying free-energy landscape being sufficiently rugged to display several low-lying metastable states; and (ii) the exceedingly slow kinetics exhibited in the solid phase, preventing a full/ergodic kinetic relaxation.

The screening of polymorphs has traditionally exclusively been performed experimentally, in spite of the significant costs involved. Computational methods hold the promise of predicting polymorphic stability before going to the laboratory. In the context of molecular crystals, especially pharmaceuticals and porous (organic) cages, a considerable body of work has recently emerged.<sup>2–13</sup> The modeling of polymorphism holds two challenges: sampling and modeling accuracy. The free-energy

landscape exhibits an overwhelming number of configurations, of which only an infinitesimal fraction competes in terms of low-lying states. Furthermore, correctly ranking the relative free energies of each conformer requires computational methods that are accurate enough (of the order of thermal energy,  $k_B T$ ) to reproduce the underlying interactions. Many methods exist to tackle these two challenges, out of which we mention the use of an appropriately-tuned force-field for sampling and electronic-structure methods (e.g., density functional theory) for energetic characterization.<sup>14–16</sup>

Here, we focus on polymers, which not only embody countless industrial applications, but also for which we critically lack a detailed picture of their free-energy landscape. Evidently, the increased number of atoms per molecule involved will lead to higher structural correlations, significantly larger barriers, and much longer timescales compared to molecular crystals of small molecules. While many semicrystalline polymers possess only a single type of unit cell, there are exceptions: syndiotactic polystyrene (sPS), for instance, is well-known for its complex crystal polymorphism.

In this work, we aim at unraveling the underlying free-energy landscape of sPS, to better understand the body of experimental evidence gathered around its polymorphs. We focus on the thermally-induced processing aspect – the  $\alpha$  and  $\beta$  polymorphs, shown in Fig. 1.<sup>18–23</sup> They share the same intrachain conformations, but with different interchain-packing structures. The  $\alpha$  and  $\beta$  forms of sPS are further classified into limiting disordered forms,  $\alpha'$  and  $\beta'$ , and limiting ordered forms,  $\alpha''$  and  $\beta''$ .<sup>18,20,22,24</sup> The processing conditions

<sup>a</sup> Max Planck Institute for Polymer Research, 55128 Mainz, Germany

<sup>b</sup> Interdisciplinary Center for Scientific Computing, University of Heidelberg, 69120 Heidelberg, Germany

<sup>c</sup> Digital Organization, Merck KGaA, 64293 Darmstadt, Germany

<sup>d</sup> Van 't Hoff Institute for Molecular Sciences and Informatics Institute, University of Amsterdam, Amsterdam 1098 XH, The Netherlands. E-mail: t.bereau@uva.nl

<sup>†</sup> Electronic supplementary information (ESI) available. See DOI: 10.1039/d0sm01342k



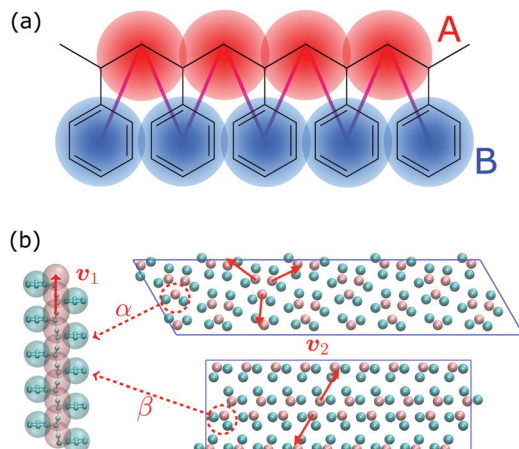


Fig. 1 (a) Molecular structure of polystyrene and the CG-mapping scheme of the Fritz model.<sup>17</sup> (b) Left: Longitudinal view of an all-trans chain conformation; Right: transverse section of the experimentally-resolved  $\alpha$  and  $\beta$  forms. In the transverse sections, each polymer chain is represented by three CG beads (highlighted in red dashed circles). The red solid lines represent cross-sectional vectors pointing from the backbone to the bisector of its two closest side chains.

impact the forms experimentally observed.<sup>22,24</sup> Fig. 1 displays the limiting ordered forms.

Experimental evidence has pointed out the strong impact of the processing conditions: starting material, initial temperature, and cooling rate.<sup>18,22,24-28</sup> They hint at a highly complex free-energy landscape. The relative stability between the  $\alpha$  and  $\beta$  polymorphs is noteworthy: (i) starting from a high initial temperature, fast (slow) cooling will lead to the  $\alpha$  ( $\beta$ ) forms; (ii) under an identical slow cooling rate, melt crystallization starting under 230 °C and above 260 °C will yield the  $\alpha$  and  $\beta$  polymorphs, respectively, while intermediate temperatures generate mixtures thereof. These results suggest that given sufficient mobility thanks to a high initial temperature and a slow enough cooling rate, the preferred packing structure corresponds to the  $\beta$  form. In the case of stiffened chains and/or reduced molecular mobility, the  $\alpha$  polymorph is preferred. These observations of the structural properties of sPS indicate that crystallization to the  $\alpha$  form results from a kinetically-controlled process, while  $\beta$  would be the thermodynamically stable form. Our understanding, therefore, falls short in several ways: how the free-energy landscape translates into the apparent differences between the two forms, and also a more mechanistic insight regarding the origin of these effects.

While computational studies of polymer crystal polymorphs remain to date extremely limited, we note the work of Tamai and co-workers on nanoporous cavity structures in the  $\alpha$  and  $\beta$  forms,<sup>29</sup> the diffusion of gases,<sup>30,31</sup> the orientational motion of guest solvents,<sup>32,33</sup> and the adsorption of small molecules.<sup>34-36</sup> These studies helped understand the structural features of some of these forms. Unfortunately, the atomistic resolution involved strongly limits the timescale that can be reached with the simulations – on the order of nanoseconds. This prevents both the observation of self assembly and also polymorph interconversion, thereby hindering access to the free-energy landscape.

To address the time-scale issue, we turn to coarse-grained (CG) modeling. By lumping several atoms into one larger superparticle or bead, CG models can sample significantly faster, while offering a systematic connection to the reference chemistry.<sup>37</sup> Some of us recently applied a structure-based CG model aimed at reproducing certain thermodynamic aspects of sPS.<sup>17</sup> Despite a parametrization and validation performed exclusively in the melt, we found remarkable transferability to the crystalline phase: not only does the CG model stabilize the  $\alpha$  and  $\beta$  polymorphs, the melting temperatures of the two phases were found to be in excellent agreement.<sup>38</sup> Our study aimed at an exploration of the self-assembly mechanisms of sPS, using a temperature-based enhanced-sampling molecular dynamics (MD) technique – parallel tempering. In the present work, we instead turn to methods based on collective variables (CVs), specifically metadynamics.<sup>39,40</sup> We will show that an appropriate choice of CVs can lead to convergence of the simulations, and offer us access to a great diversity of structural forms. We present for the first time the free-energy landscape of polymorphism of a polymer crystal.

We further challenge the calculations of the free-energy difference between  $\alpha$  and  $\beta$  polymorph stability by means of quantum-chemical calculation at the density functional theory (DFT) level. The results show excellent agreement with the CG simulations given the change in resolution. Critically, we find in both cases the preferential stabilization of the  $\beta$  phase – in line with experiments.

## II. Results and discussion

### A. Metadynamics

In the Methods section, we present collective variables (CVs) that are capable of distinguishing five different phases of sPS (Section IV B). A significant distinction between these phases is essential to also enable the discovery of other intermediate phases. A further requirement is the absence of hidden barriers that would hinder dynamics along the CVs.<sup>39</sup> To alleviate possible artifacts due to an inappropriate choice of CVs, we tested several of them and later re-weighted all simulations to the same CV space. This further allows us to empirically check the convergence of our simulations.

We focus on a two-dimensional CV exploration, as a balance between exploration and convergence: a three-dimensional CV-space exploration can require excessive memory and presents challenges to converge due to the curse of dimensionality. We note that extensions of the method, such as bias-exchange and parallel-bias metadynamics, can help along these lines.<sup>41-44</sup> We herein present four combinations of CVs (referenced in Table S1, ESI†) based on orientational features between the  $v_2$  transverse vectors (Fig. 1b). Variants of  $\mathcal{S}$  focus on specific angles, while the second Legendre polynomial  $P_2$  probes the overall ordering: (i)  $\Delta\mathcal{S} & \mathcal{S}_1$ ; (ii)  $\Delta\mathcal{S} & \mathcal{S}_2$ ; (iii)  $\Delta\mathcal{S} & \mathcal{S}_3$ ; (iv)  $\Delta\mathcal{S} & P_2(v_2)$ .

Fig. 2 shows a metadynamics simulation at  $T = 400$  K driven by the combination of CVs  $\Delta\mathcal{S} & P_2(v_2)$  using two walkers. The walkers were initiated from the two crystalline phases  $\alpha$  and  $\beta$ .

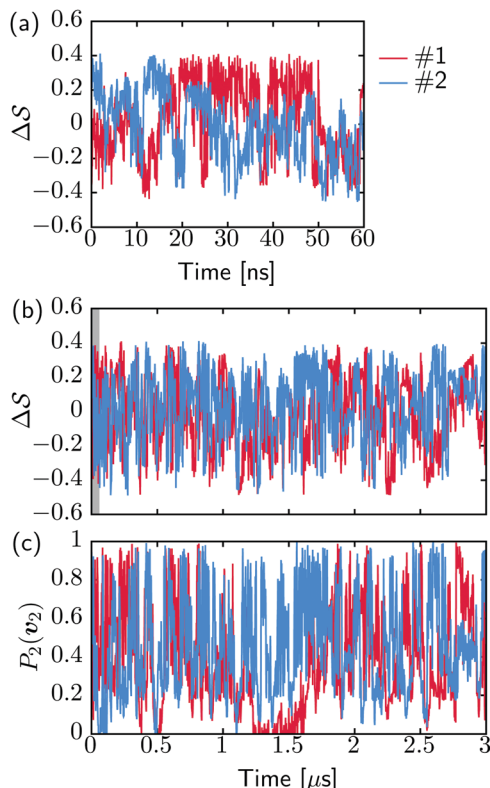


Fig. 2 Time evolution of the CVs during two metadynamics runs (each walker shown with a different color) using the combination of (b)  $\Delta S$  & (c)  $P_2(v_2)$ . (a) First 60 ns of  $\Delta S$ , represented by a gray area in panel b.

The simulations are able to transition many times between the main polymorphs, starting at around 20 ns (Fig. 2a). The results highlight that the ability of the CVs to distinguish  $\alpha$  from  $\beta$  helps ensure large conformational transitions (Fig. S2, ESI<sup>†</sup>). We note however the absence of conformations in the amorphous phase, due to both our sampling below the transition temperature (roughly 450 K) and our protocol's restraining box range and chain direction (see Section IV C).

## B. Polymorphic stability

Having established that our combination of CVs enables a satisfactory transition between major polymorphs, we turn to the question of convergence. To assess convergence, we run metadynamics in the CV space of our four combinations, and marginalize the free-energy landscape to only display their common CV: the SMAC difference  $\Delta S$ . Fig. 3 compares the free-energy surface as a function of the CV  $G(\Delta S)$ . We have marked the  $\alpha$  and  $\beta$  polymorphs according to values of the CV from unbiased MD simulations (see the ESI<sup>†</sup>). All four curves agree within roughly 5 kJ mol<sup>-1</sup> across the range of  $\Delta S$  values, despite their sampling along different complementary CVs. Convergence as a function of simulation time is further displayed in Fig. 4a, which focuses on the free-energy difference between the  $\alpha$  and  $\beta$  polymorphs,  $G_\alpha - G_\beta$ . We find that all curves converge after roughly 1 to 2  $\mu$ s. We do see variations between simulations reminiscent of the spread in panel (a).

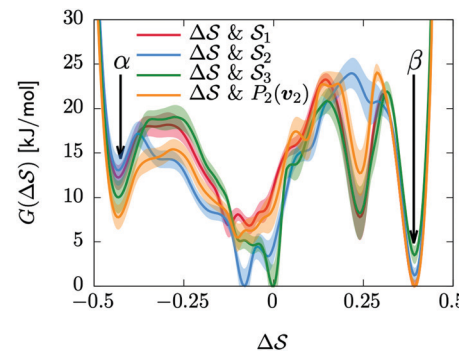


Fig. 3 Convergence of the free-energy calculations. Comparison of four metadynamics simulations at  $T = 400$  K with different CVs (see labels) projected on  $\Delta S$ .

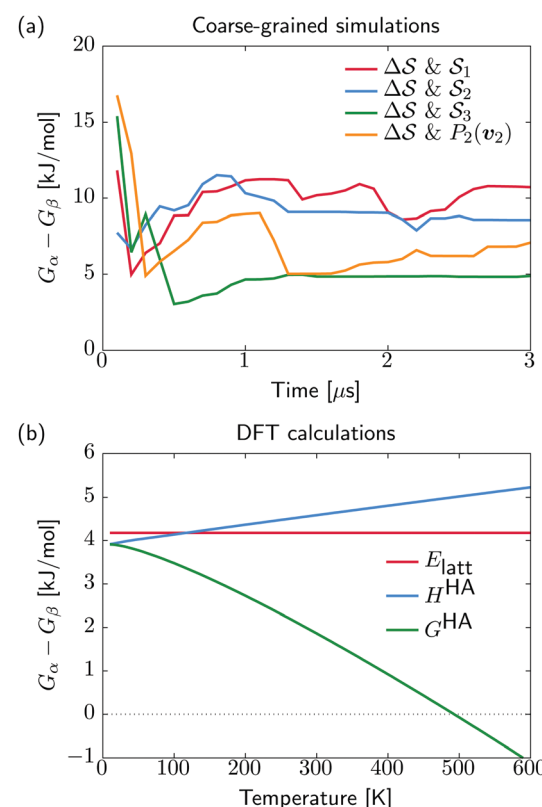


Fig. 4 Free-energy difference between  $\alpha$  and  $\beta$  forms. (a) The CG simulations show the time evolution of  $G_\alpha - G_\beta$  from the different metadynamics simulations. (b) The DFT-based stability differences at standard pressure and as a function of temperature, including lattice energy  $E_{\text{latt}}$ , enthalpy  $H^{\text{HA}}$ , and free energy  $G^{\text{HA}}$ .

Given the remarkable complexity of probing the free-energy landscape of polymer crystals, we consider this level of agreement as an encouraging indicator of the level of convergence of our simulations.

Metadynamics simulations on different system sizes lead to similar free-energy profiles (see Fig. S5, ESI<sup>†</sup>), whether changing the number of chains in the box or the number of monomers per chain. We rationalize the lack of system-size

dependence in two ways: (i) the lack of dependence on the number of chains can be explained by the collective nature of the transitions, where the box is so small that all chains transition to a new phase at once; and (ii) the free-energy barriers do not scale with the number of monomers, because the transitions are orthogonal to the chain direction, as indicated by the order parameters  $P_2(v_1)$  and  $P_2(v_2)$  (see Fig. S2, ESI†). As such, the size regime we work with appears to have a lack of system-size dependency, despite the extensivity of the free energy. Identifying this scaling would require the simulation of much larger simulation boxes, for instance because multiple structures could occur (concurrent with grain boundaries).

Having identified the two polymorphs as local minima with a rationalization of kinetic routes in between them, we try to further establish their relative thermodynamic stability. For this, we start from the experimentally determined structures and employ quantum mechanical methods for local structure relaxations and prediction of their temperature dependent free energy (see Section IV D). In contrast to the molecular dynamics simulations, our DFT results do not describe anharmonicities of the energy surface, potentially neglecting some thermal effects. On the other hand, the described interactions are at a quantum-mechanical level, physically more sound, and thus

expected to be more accurate compared to the classical potentials used in our molecular dynamics. We note that while the  $\alpha$  and  $\beta$  polymorphs for the quantum-mechanical calculations are taken from experimental structures, the coarse-grained references stem from the simulations. Our recent analysis of the CG model indicated a faithful stabilization of the  $\alpha$  structure but discrepancies in the  $\beta$  structure, likely due to side-chain packing issues.<sup>38</sup> Using experimental and simulation  $\beta$  structures for the quantum-mechanical calculations and CG simulations, respectively, allows us to account for the limited resolution of the CG model.

We show in Fig. 4b the quantum-mechanical energy difference between the two polymorphic forms. In a static picture at 0 K, sPS  $\beta$  is predicted to be more stable by 4 kJ mol<sup>-1</sup>. Upon heating to 400 K, the enthalpy difference increases by 1 kJ mol<sup>-1</sup>, while the free energy difference decreases by 3 kJ mol<sup>-1</sup>. At elevated temperatures of about 500 K, form  $\alpha$  is predicted to be more stable, which is, however, not experimentally observable due to the amorphous phase. The stability difference at room temperature is in excellent agreement with the estimations from our dynamics simulations, indicating a stabilization of  $\beta$  by 5–10 kJ mol<sup>-1</sup>. The smaller stability difference predicted by DFT is in line with our experience from

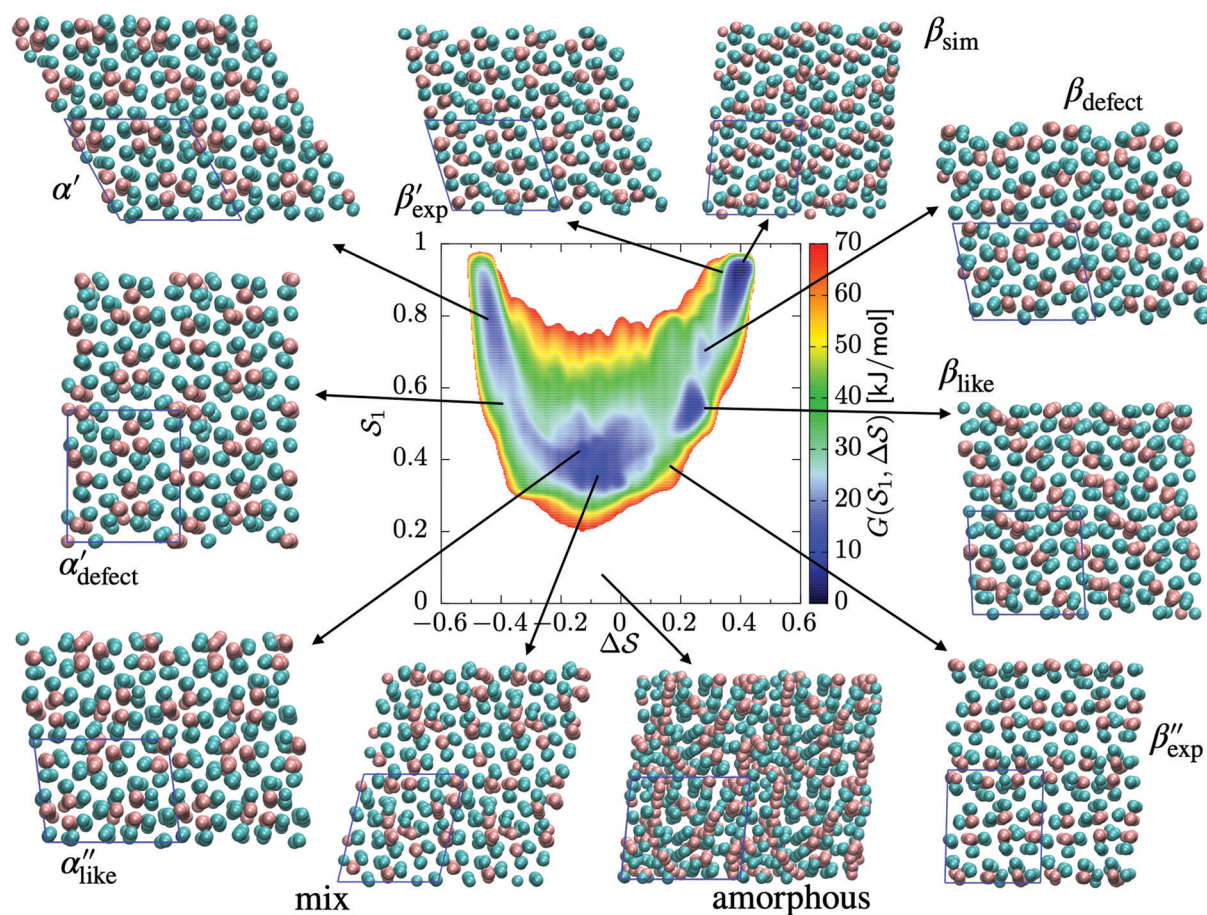


Fig. 5 Free-energy landscape of sPS sampled with metadynamics as a function of the CVs:  $G(S_1, \Delta S)$ . Various structures – representative of the simulations and/or the experiments – are displayed and identified on the surface.



molecular crystals, where higher quality interaction energy models typically lead to smaller energy gaps between polymorphs.<sup>14</sup> The overall analysis matches the experimental expectation that form  $\alpha$  crystallizes on rapid cooling from elevated temperatures, while  $\beta$  forms in slow cooling experiments.<sup>45</sup>

The analysis reported in Fig. 4 shows that the  $\beta$  form is systematically better stabilized than the competing  $\alpha$  form. The 1D landscape clearly separates  $\alpha$  from  $\beta$  at the left and right sides of the range, respectively. These are separated by both  $\alpha/\beta$  mixtures and the amorphous phases at around  $\Delta S \approx 0$ . Interestingly, we observe a significantly lower free-energy barrier upon going from the amorphous phase to the pure  $\alpha$  polymorph, compared to that for the  $\beta$  polymorph: while the former is between 10 and 15  $\text{kJ mol}^{-1}$  high, the other is up to 20  $\text{kJ mol}^{-1}$ . The  $\beta$  form is more stable across the CV space, but the  $\alpha$  form is easier to obtain from the mixture and amorphous phases – a kinetic effect. This can help rationalize the kinetic-trap behavior of the  $\alpha$  form found experimentally.<sup>45</sup> Some of us previously identified an overpopulation of the  $\alpha$  form when probed in simulation box geometries concomitant to the  $\alpha$  unit cell, suggesting a templating mechanism.<sup>38</sup>

### C. Free-energy landscape of sPS

As an extension to Fig. 3, Fig. 5 shows a representation of the free-energy landscape for the CV combination  $\Delta S & S_1$ . Stability is color coded from blue to red. We observe a large diversity of phases with distinct structural features. Notably, we find many more structures than our previous study based on parallel tempering.<sup>38</sup>

We first analyze structures similar to the  $\alpha$  polymorph. Of particular interest are symmetries around triplets of chains that form the fundamental symmetric unit of  $\alpha$  structures (see Fig. 1b). As compared to our previous work that used parallel tempering, we observe a broader variety of relative orientations between chain triplets. Small but noticeable variations can be found among the  $\alpha$ -type structures on the landscape. The differentiation between  $\alpha'$  and  $\alpha''$  is made more difficult by imposing 12 chains in our simulation box, while the unit cell of  $\alpha$  contains only 9 chains.<sup>20</sup> We emphasize the difference between apparently distinct forms stabilized in our simulations:  $\alpha'$ ,  $\alpha'_{\text{defect}}$  and  $\alpha''_{\text{defect}}$ , shown in Fig. 5. All triplets of chains, represented by groups of tan-colored beads, exhibit virtually identical orientations in  $\alpha'$  and little variation in  $\alpha'_{\text{defect}}$ : the angles between side-chain vectors are almost all strictly at 120°, leading to  $\Delta S \approx -0.4$ .  $\alpha''_{\text{like}}$ , on the other hand, displays two different triplet orientations, analogous to the experimentally resolved  $\alpha''$ . The angles between side-chain vectors do not always correspond to 120°, leading to  $\Delta S \approx -0.2$ , located near the mixture phases. Our simulations do not stabilize the  $\alpha''$  polymorph, which may be due to the number of chains being incongruent with the unit cell, or possibly limitations in the CG force field in reproducing fine steric features.<sup>17,38</sup>

In line with our previous study, we find an alternate form to the experimentally-resolved<sup>22,24</sup> limiting disordered  $\beta'$  and limiting ordered  $\beta''$  polymorphs as the most global minimum

of sPS:  $\beta_{\text{sim}}$ , where we highlighted the difference in layering.<sup>38</sup> While the parallel tempering simulations led to neither experimental form, the metadynamics simulations successfully sampled them, albeit at too high free energy: the  $\beta'_{\text{exp}}$  and  $\beta''_{\text{exp}}$  forms sit at about 30 and 50  $\text{kJ mol}^{-1}$  higher than the global minimum, respectively. We argued before that the simple description of the side-chain sterics likely had a detrimental effect on the stability of the  $\beta$  polymorphs. This effect was motivated by a discrepancy in the melting temperature from CG simulations, as compared to reference atomistic simulations: in excellent agreement for the  $\alpha$  form, but with too-low stability for  $\beta$ . In the context of the present work, these structural artifacts likely give rise to shifts in the free-energy landscape shown in Fig. 5.

## III. Conclusion

In this paper, we study the free-energy landscape of syndiotactic polystyrene (sPS) using computational methods to get microscopic insight into polymorphic interconversion. The development of adequate collective variables (CVs) applied to metadynamics, together with the use of a remarkably transferable coarse-grained (CG) model, allows us for the first time to cross the significant barriers between polymorphs in polymer crystals. Minute structural differences between polymorphs require finely-tuned CVs to account for the small variations. Rather than relying on a single CV combination, running metadynamics simulations on several such combinations and re-weighting them help us test for convergence of the simulations. We find excellent agreement between four such combinations, despite the significant barriers exerted by the system.

We rely on a combination of two different SMAC variables<sup>46</sup> to build a free-energy landscape. The  $\beta$  form clearly stands as the global minimum, even though we observe fine differences between the simulated and experimental layerings, arguably an artifact of the side-chain representation in the CG model. Encouragingly, we do observe the two experimental  $\beta'_{\text{exp}}$  and  $\beta''_{\text{exp}}$  structures in the metadynamics runs. The  $\alpha$  form is between 5 and 10  $\text{kJ mol}^{-1}$  less stable than the global minimum. As a complementary approach, we used quantum mechanical models to compute the temperature dependent relative stability of the  $\alpha$  and  $\beta$  polymorphs. We predict the stability to be slightly smaller (1  $\text{kJ mol}^{-1}$ ), but can overall confirm the CG simulations.

Remarkably, we find a significantly lower free-energy barrier upon going from the amorphous phase to  $\alpha$  rather than  $\beta$ . This lowered activation could partially explain the  $\alpha$  polymorph's tendency to be identified as a kinetic trap. It also complements our previous observation:  $\alpha$  is overstabilized in box geometries congruent with its unit cell, a templating mechanism of sorts. Differences in nucleation rates may further help drive the system in the direction of  $\alpha$ , although this is beyond the scope of this work.

Varying the system size will naturally affect the results: smaller simulation boxes are more likely to suffer from incompatibilities with different crystal units, resulting in artificially



low stabilization. On the other hand, the significant free-energy barriers will become more challenging to cross as simulation boxes grow. The present study demonstrates that a multiscale approach can provide insight and complementary information to experiments on polymer-crystal polymorphism.

## IV. Simulation methods

### A. Coarse-grained simulations

We rely on a previously-developed coarse-grained (CG) model for syndiotactic polystyrene (sPS), referred to hereafter as the Fritz model.<sup>17</sup> It maps each monomer onto two types of CG beads: “A” for the chain backbone and “B” for the phenyl ring (Fig. 1a). The model represents PS as a linear chain of alternating A and B CG beads, supplemented by sophisticated bonded potentials to ensure accurate structures, including the correct tacticity – enabling the crystallization of sPS. The bonded interactions were obtained by direct Boltzmann inversion of distributions obtained from atomistic simulations of single chains in a vacuum. The nonbonded potentials are derived using the conditional reversible work (CRW) method:<sup>47,48</sup> constrained-dynamics runs with the all-atom model of two short chains in a vacuum.

### B. Collective variables

Metadynamics acts on the selected CVs to drive the system and cross free-energy barriers. This puts an essential emphasis on the choice of CVs, known to be extremely system and process dependent.<sup>39</sup> A large variety of CVs have been used, for instance, distances, angles, or dihedrals formed by atoms or groups of atoms,<sup>49</sup> coordination numbers,<sup>41,50,51</sup> and Steinhardt parameters.<sup>52–54</sup>

Crystallization is typically characterized by long-range order. For example, cluster symmetries are often probed *via* the Steinhardt parameter,  $Q_l$ ,<sup>55,56</sup> which represents the rotationally-invariant spherical harmonics of order  $l$ .  $Q_4$  and  $Q_6$ , in particular, have been studied in the context of Lennard-Jones particles,<sup>52</sup> ice,<sup>53</sup> and calcium carbonate nanoparticles.<sup>54</sup> To study polymorphism in sPS, however, we have found the Steinhardt parameter to inefficiently distinguish crystalline forms (see Fig. S3, ESI†). We rationalize this by the lack of differentiation for transverse vectors (see Fig. 1b). This has led us to the development of CVs that are tailored to sPS.

Fig. 1b shows a longitudinal view of a chain conformation, as well as transverse sections of the two main polymorphs of interest: the experimentally-determined  $\alpha$  and  $\beta$  structures.<sup>24</sup> We herein propose two sets of vectors: one longitudinal vector,  $\mathbf{v}_1$ , and one transverse vector,  $\mathbf{v}_2$ .  $\mathbf{v}_1$  is oriented along the backbone, and it is defined as the interparticle vector between two consecutive monomers (*i.e.*, backbone beads). As for the transverse vector  $\mathbf{v}_2$ , for each monomer, it originates from the second backbone and points to the bisector of the two closest side chains. Fig. 1b indicates that typical angles for the  $\alpha$  and  $\beta$  polymorphs are roughly  $120^\circ$  and  $180^\circ$ , respectively. Note that here, to improve the efficiency of computation, the side-chain

vector is an average over each whole molecule. Effectively this assumes a homogeneous configuration across the chain, in line with the system sizes considered here.

Because these two polymorphs consist of identical chain conformations, no differences can be extracted from *intrachain* statistics. Instead, differences between polymorphs are concentrated in the *interchain* configurations. As such, any CV that is able to distinguish between polymorphs ought to focus on interchain geometries. By symmetry, the most noticeable differences occur along the transverse sections. These differences can be displayed more intuitively by the distribution of angles between neighboring transverse vectors  $\mathbf{v}_2$  (see Fig. S1, ESI†), which is derived from unbiased MD simulations at 300 K. In the following discussion, we will introduce two kinds of CVs that are functions of these transverse angles.

**1. Legendre polynomial  $P_2$ .** The second Legendre polynomial  $P_2$  probes the orientation between two vectors  $\mathbf{e}_i$  and  $\mathbf{e}_j$ :

$$P_2(\mathbf{e}) = \frac{3}{2}(\mathbf{e}_i \cdot \mathbf{e}_j)^2 - \frac{1}{2}. \quad (1)$$

$P_2$  is a natural candidate to describe orientational ordering and has been used to monitor the crystalline growth and/or state of polymer chains.<sup>57,58</sup> Some of us previously used  $P_2$  to monitor the melting transition of sPS.<sup>38</sup>

**2. SMAC.** Giberti *et al.*<sup>46</sup> recently introduced a CV to capture the inherent variety of crystal symmetries.<sup>59</sup> This CV, simply called SMAC in Plumed, was formulated with the aim of accounting for both local density and the mutual orientation of molecules. In our case, it probes features of the angle distributions between transverse vectors, as shown in Fig. S1 (ESI†). It compares an input angle,  $\theta_{ij}$ , with a reference angle,  $\theta_n$ , *via*

$$K_n(\theta_{ij} - \theta_n) = e^{-(\theta_{ij} - \theta_n)^2 / 2\sigma_n^2}. \quad (2)$$

This kernel smoothly interpolates from identical to distant angles leading to values from 1 to 0, respectively. SMAC relies on these kernels to probe one or multiple reference angles according to the phase of interest, supplemented by a smooth cutoff scheme:

$$s_i = \frac{\left\{ 1 - \psi \left[ \sum_{j \neq i} \sigma(r_{ij}) \right] \right\} \sum_{j \neq i} \sigma(r_{ij}) \sum_n K_n(\theta_{ij} - \theta_n)}{\sum_{j \neq i} \sigma(r_{ij})}. \quad (3)$$

Eqn (3) relies on the two switching functions  $\sigma(r) = \frac{1 - (r/r_\sigma)^6}{1 - (r/r_\sigma)^{12}}$  and  $\psi(r) = \exp(-r/r_\psi)$ , where  $r_\sigma$  and  $r_\psi$  (see Table S1, ESI†) provide a balance to keep the CV local, while incorporating enough numbers. The quantity is then averaged over all  $s_i$ :

$$\mathcal{S} = \sum_{i=1}^N s_i / N.$$

Based on the angle distributions of Fig. S1 (ESI†), we construct a number of SMAC CVs using various sets of reference angles to optimally distinguish between sPS phases. Table S1 (ESI†) lists the set of CVs we used in this work. For instance, the main peaks for the  $\alpha$  and  $\beta$  phases led to the definition of SMAC CVs  $S_\alpha$  and  $S_\beta$ , centered at  $120^\circ$  and  $170^\circ$ , respectively.

To emphasize both features at once, we constructed a CV based on their difference:  $\Delta\mathcal{S} = \mathcal{S}_\beta - \mathcal{S}_\alpha$ . This can be observed by monitoring the CV during unbiased MD simulations (Fig. S2c, ESI<sup>†</sup>). Three additional SMAC CVs are presented in Table S1 (ESI<sup>†</sup>).

### C. Metadynamics

Well-tempered metadynamics simulations were performed at 400 K.<sup>40,60–65</sup> The bias deposition stride was set to be 0.5 ps, and the bias factor was 20. The Gaussian-bias width was set to 0.01 for  $\Delta\mathcal{S}$ , and 0.05 otherwise. The initial Gaussian heights were all set to 3 kJ mol<sup>-1</sup>. Each simulation consisted of multiple walkers.<sup>66</sup> In metadynamics, we refer to a biased run that explores the CV-space as a walker, while multiple walkers simultaneously explore and carve the same free-energy landscape. This method can significantly speed up the convergence of the simulations, as all walkers contribute to a single, combined free-energy landscape. In this work, 2 walkers were run in parallel and initialized from the  $\alpha$  and  $\beta$  forms, respectively. All simulations were performed using GROMACS 5.1.4<sup>67</sup> and PLUMED 2.4.<sup>68,69</sup> Simulations were carried out in the isothermal-isobaric ensemble at  $P = 1$  bar using the velocity-rescale thermostat<sup>70</sup> and the anisotropic Parrinello-Rahman barostat.<sup>71</sup> We ensured stable variations in the simulation box by restraining the range of allowed geometries ( $5 < a^2 < 9$ ;  $5 < b^2 < 9$ ;  $6 < c^2 < 8$  nm<sup>2</sup>). We also restrained the direction of each chain to lie within 30° of the box's  $z$  component. This avoided significant collective rotations of the chains with respect to the simulation box, leading to alignments along the other coordinates. Such a scheme merely aims at forcing all chains to loosely lie within an arbitrarily-chosen  $z$  axis. This helped avoid artifacts when calculating longitudinal and transverse vectors, especially at higher temperatures. More details can be found in the ESI.<sup>†</sup>

### D. Quantum-chemical methods

Quantum-chemical methods are used to simulate the relative thermodynamical stability of the two sPS polymorphs. The two polymorphic forms identified by the metadynamics simulations and experimentally characterized in the literature have been taken as starting points for local geometry optimization. Phonon modes are computed to confirm the stationary points as local minima and to give access to the temperature-dependent harmonic Gibbs free energy

$$G^{\text{HA}}(T, P) = E_{\text{latt}} + G_{\text{vib}}^{\text{HA}}(T) + PV. \quad (4)$$

Here,  $E_{\text{latt}}(V)$  is the zero-temperature internal energy of the crystal given per monomer unit—the lattice energy. The vibrational contributions are

$$G_{\text{vib}}^{\text{HA}}(T) = \sum_{\mathbf{k}, p} \frac{\hbar\omega_{\mathbf{k}, p}}{2} + k_{\text{B}}T \sum_{\mathbf{k}, p} \left[ \ln \left( 1 - e^{-\frac{\hbar\omega_{\mathbf{k}, p}}{k_{\text{B}}T}} \right) \right], \quad (5)$$

where the phonon frequencies  $\omega_{\mathbf{k}, p}$  correspond to a  $\mathbf{k}$ -point in the first Brillouin zone and a phonon band index  $p$ . The temperature-dependent harmonic enthalpy,  $H^{\text{HA}}$ , is described in the ESI.<sup>†</sup> The quantum chemical calculations are performed

using density functional theory (DFT), which is the method of choice for many materials applications due to its favorable accuracy to computational cost ratio.<sup>72–75</sup> The DFT calculations are done with a screened exchange hybrid density functional, dubbed HSE-3c.<sup>76,77</sup> It combines accurate descriptions of geometries over a broad class of systems with an efficient treatment of non-local exchange and long-range London dispersion interaction.<sup>78,79</sup> For a general overview of dispersion corrections in the density functional framework and the treatment of molecular crystals, see ref. 80–82. The implementation of HSE-3c into the CRYSTAL17 program enables the fast computation of electronic structures and phonon modes using all point- and space-group symmetries.<sup>83,84</sup> Geometry optimizations are performed with tight convergence thresholds and in space groups  $P3_1(\alpha)$  and  $Pnma(\beta)$ . The Brillouin zone has been sampled with a  $1 \times 1 \times 5$  and  $1 \times 5 \times 3$  grid for the  $\alpha$  and  $\beta$  polymorphs, respectively.  $\Gamma$ -Point frequencies have been computed by SHF-3c,<sup>85,86</sup> and the above  $\Gamma$ -point frequencies are found to be negligible at the DFTB3-D3 level,<sup>87–89</sup> which has been shown to be a reliable approach for organic solids.<sup>90</sup>

## Conflicts of interest

There are no conflicts to declare.

## Acknowledgements

We thank Christine Peter for insightful discussions, as well as Bingqing Cheng, Robinson Cortes-Huerto, and Hsiao-Ping Hsu for critical reading of the manuscript. CL was supported by the Max Planck Graduate Center. TB was partially supported by the Emmy Noether program of the Deutsche Forchungsgemeinschaft (DFG). Open Access funding provided by the Max Planck Society.

## References

- 1 H. G. Brittain, *et al.*, Polymorphism in pharmaceutical solids, *Drugs Pharm. Sci.*, 1999, **95**, 183–226.
- 2 R. J. Gdanitz, *Ab initio* prediction of molecular crystal structures, *Curr. Opin. Solid State Mater. Sci.*, 1998, **3**(4), 414–418.
- 3 J. Bernstein and J. M. Bernstein, *Polymorphism in Molecular Crystals*, Oxford University Press, vol. 14, 2002.
- 4 M. Jansen, K. Doll and J. Christian Schön, Addressing chemical diversity by employing the energy landscape concept, *Acta Crystallogr., Sect. A: Found. Crystallogr.*, 2010, **66**(5), 518–534.
- 5 J. T. A. Jones, T. Hasell, X. Wu, J. Bacsá, K. E. Jelfs, M. Schmidtmann, S. Y. Chong, D. J. Adams, A. Trewin, F. Schiffman, F. Cora, B. Slater, A. Steiner, G. M. Day and A. I. Cooper, Modular and predictable assembly of porous organic molecular crystals, *Nature*, 2011, **474**(7351), 367–371.
- 6 Y. A. Abramov, Current computational approaches to support pharmaceutical solid form selection, *Org. Process Res. Dev.*, 2012, **17**(3), 472–485.



7 E. O. Pyzer-Knapp, H. P. G. Thompson, F. Schiffmann, K. E. Jelfs, S. Y. Chong, M. A. Little, A. I. Cooper and G. M. Day, Predicted crystal energy landscapes of porous organic cages, *Chem. Sci.*, 2014, **5**(6), 2235–2245.

8 A. J. Cruz-Cabeza, S. M. Reutzel-Edens and J. Bernstein, Facts and fictions about polymorphism, *Chem. Soc. Rev.*, 2015, **44**(23), 8619–8635.

9 M. A. Neumann, J. van de Streek, F. P. A. Fabbiani, P. Hidber and O. Grassmann, Combined crystal structure prediction and high-pressure crystallization in rational pharmaceutical polymorph screening, *Nat. Commun.*, 2015, **6**, 7793.

10 S. L. Price and S. M. Reutzel-Edens, The potential of computed crystal energy landscapes to aid solid-form development, *Drug Discovery Today*, 2016, **21**(6), 912–923.

11 S. L. Price and J. G. Brandenburg, Molecular crystal structure prediction, in *Non-Covalent Interactions in Quantum Chemistry and Physics*, Elsevier, 2017, pp. 333–363.

12 A. Pulido, L. Chen, T. Kaczorowski, D. Holden, M. A. Little, S. Y. Chong, B. J. Slater, D. P. McMahon, B. Bonillo, C. J. Stackhouse, A. Stephenson, C. M. Kane, R. Clowes, T. Hasell, A. I. Cooper and G. M. Day, Functional materials discovery using energy–structure–function maps, *Nature*, 2017, **543**(7647), 657–664.

13 G. M. Day and A. I. Cooper, Energy-structure-function maps: Cartography for materials discovery, *Adv. Mater.*, 2017, **30**(37), 1704944.

14 A. M. Reilly, R. I. Cooper, C. S. Adjiman, S. Bhattacharya, A. D. Boese, J. G. Brandenburg, P. J. Bygrave, R. Bylsma, J. E. Campbell and R. Car, *et al.*, Report on the sixth blind test of organic crystal structure prediction methods, *Acta Crystallogr., Sect. B: Struct. Sci., Cryst. Eng. Mater.*, 2016, **72**(4), 439–459.

15 N. Marom, R. A. DiStasio, V. Atalla, S. Levchenko, A. M. Reilly, J. R. Chelikowsky, L. Leiserowitz and A. Tkatchenko, Many-body dispersion interactions in molecular crystal polymorphism, *Angew. Chem., Int. Ed.*, 2013, **52**(26), 6629–6632.

16 J. Hoja, H.-Y. Ko, M. A. Neumann, R. Car, R. A. DiStasio and A. Tkatchenko, Reliable and practical computational description of molecular crystal polymorphs, *Sci. Adv.*, 2019, **5**(1), eaau338.

17 D. Fritz, V. A. Harmandaris, K. Kremer and N. F. A. van der Vegt, Coarse-grained polymer melts based on isolated atomistic chains: simulation of polystyrene of different tacticities, *Macromolecules*, 2009, **42**(19), 7579–7588.

18 C. De Rosa, G. Guerra, V. Petraccone and P. Corradini, Crystal structure of the  $\alpha$ -form of syndiotactic polystyrene, *Polym. J.*, 1991, **23**(12), 1435.

19 P. Corradini, C. De Rosa, G. Guerra, R. Napolitano, V. Petraccone and B. Pirozzi, Conformational and packing energy of the crystalline  $\alpha$  modification of syndiotactic polystyrene, *Eur. Polym. J.*, 1994, **30**(10), 1173–1177.

20 C. De Rosa, Crystal structure of the trigonal modification ( $\alpha$  form) of syndiotactic polystyrene, *Macromolecules*, 1996, **29**(26), 8460–8465.

21 L. Cartier, T. Okihara and B. Lotz, The  $\alpha$  superstructure of syndiotactic polystyrene: A frustrated structure, *Macromolecules*, 1998, **31**(10), 3303–3310.

22 C. De Rosa, M. Rapacciulo, G. Guerra, V. Petraccone and P. Corradini, On the crystal structure of the orthorhombic form of syndiotactic polystyrene, *Polymer*, 1992, **33**(7), 1423–1428.

23 Y. Chatani, Y. Shimane, T. Ijitsu and T. Yukinari, Structural study on syndiotactic polystyrene: 3. crystal structure of planar form i, *Polymer*, 1993, **34**(8), 1625–1629.

24 G. Guerra, V. M. Vitagliano, C. De Rosa, V. Petraccone and P. Corradini, Polymorphism in melt crystallized syndiotactic polystyrene samples, *Macromolecules*, 1990, **23**(5), 1539–1544.

25 Y. S. Sun and E. M. Woo, Relationships between polymorphic crystals and multiple melting peaks in crystalline syndiotactic polystyrene, *Macromolecules*, 1999, **32**(23), 7836–7844.

26 E. M. Woo, Y. S. Sun and M. Lu Lee, Crystal forms in cold-crystallized syndiotactic polystyrene, *Polymer*, 1999, **40**(15), 4425–4429.

27 R. H. Lin and E. M. Woo, Melting behavior and identification of polymorphic crystals in syndiotactic polystyrene, *Polymer*, 2000, **41**(1), 121–131.

28 Y.-S. Sun and E. M. Woo, Morphology and crystal structure of cold-crystallized syndiotactic polystyrene, *Polymer*, 2001, **42**(5), 2241–2245.

29 Y. Tamai and M. Fukuda, Nanoscale molecular cavity in crystalline polymer membranes studied by molecular dynamics simulation, *Polymer*, 2003, **44**(11), 3279–3289.

30 G. Milano, G. Guerra and F. Müller-Plathe, Anisotropic diffusion of small penetrants in the  $\delta$  crystalline phase of syndiotactic polystyrene: a molecular dynamics simulation study, *Chem. Mater.*, 2002, **14**(7), 2977–2982.

31 Y. Tamai and M. Fukuda, Fast one-dimensional gas transport in molecular capillary embedded in polymer crystal, *Chem. Phys. Lett.*, 2003, **371**(1–2), 217–222.

32 Y. Tamai and M. Fukuda, Reorientational dynamics of aromatic molecules clathrated in  $\delta$  form of crystalline syndiotactic polystyrene, *Chem. Phys. Lett.*, 2003, **371**(5–6), 620–625.

33 Y. Tamai, Y. Tsujita and M. Fukuda, Reorientational relaxation of aromatic molecules in the molecular cavity of crystalline syndiotactic polystyrene studied by molecular dynamics simulation, *J. Mol. Struct.*, 2005, **739**(1–3), 33–40.

34 S. Figueroa-Gerstenmaier, C. Daniel, G. Milano, G. Guerra, O. Zavorotynska, J. G. Vitillo, A. Zecchina and G. Spoto, Storage of hydrogen as a guest of a nanoporous polymeric crystalline phase, *Phys. Chem. Chem. Phys.*, 2010, **12**(20), 5369–5374.

35 S. Figueroa-Gerstenmaier, C. Daniel, G. Milano, J. G. Vitillo, O. Zavorotynska, G. Spoto and G. Guerra, Hydrogen adsorption by  $\delta$  and  $\epsilon$  crystalline phases of syndiotactic polystyrene aerogels, *Macromolecules*, 2010, **43**(20), 8594–8601.

36 L. Sanguigno, F. Cosentino, D. Larobina and G. Mensitieri, Molecular simulation of carbon dioxide sorption in nanoporous crystalline phase of syndiotactic polystyrene, *Soft Mater.*, 2011, **9**(2–3), 169–182.

37 W. G. Noid, Perspective: Coarse-grained models for biomolecular systems, *J. Chem. Phys.*, 2013, **139**(9), 09B201\_1.



38 C. Liu, K. Kremer and T. Bereau, Polymorphism of syndiotactic polystyrene crystals from multiscale simulations, *Adv. Theor. Simul.*, 2018, **1**(7), 1800024.

39 A. Laio and F. L. Gervasio, Metadynamics: a method to simulate rare events and reconstruct the free energy in biophysics, chemistry and material science, *Rep. Prog. Phys.*, 2008, **71**(12), 126601.

40 O. Valsson, P. Tiwary and M. Parrinello, Enhancing important fluctuations: Rare events and metadynamics from a conceptual viewpoint, *Annu. Rev. Phys. Chem.*, 2016, **67**(1), 159–184.

41 S. Piana and A. Laio, A bias-exchange approach to protein folding, *J. Phys. Chem. B*, 2007, **111**(17), 4553–4559.

42 F. Marinelli, F. Pietrucci, A. Laio and S. Piana, A kinetic model of trp-cage folding from multiple biased molecular dynamics simulations, *PLoS Comput. Biol.*, 2009, **5**(8), e1000452.

43 F. Baftizadeh, P. Cossio, F. Pietrucci and A. Laio, Protein folding and ligand-enzyme binding from bias-exchange metadynamics simulations, *Curr. Phys. Chem.*, 2012, **2**(1), 79–91.

44 J. Pfaendtner and M. Bonomi, Efficient sampling of high-dimensional free-energy landscapes with parallel bias metadynamics, *J. Chem. Theory Comput.*, 2015, **11**(11), 5062–5067.

45 E. M. Woo, Y.-S. Sun and C.-P. Yang, Polymorphism, thermal behavior, and crystal stability in syndiotactic polystyrene vs. its miscible blends, *Prog. Polym. Sci.*, 2001, **26**(6), 945–983.

46 F. Giberti, M. Salvalaglio, M. Mazzotti and M. Parrinello, Insight into the nucleation of urea crystals from the melt, *Chem. Eng. Sci.*, 2015, **121**, 51–59.

47 E. Brini, V. Marcon and N. F. A. van der Vegt, Conditional reversible work method for molecular coarse graining applications, *Phys. Chem. Chem. Phys.*, 2011, **13**(22), 10468–10474.

48 G. Deichmann and N. F. A. van der Vegt, Conditional reversible work coarse-grained models of molecular liquids with coulomb electrostatics-a proof of concept study on weakly polar organic molecules, *J. Chem. Theory Comput.*, 2017, **13**(12), 6158–6166.

49 F. L. Gervasio, A. Laio and M. Parrinello, Flexible docking in solution using metadynamics, *J. Am. Chem. Soc.*, 2005, **127**(8), 2600–2607.

50 G. Bussi, F. Luigi Gervasio, A. Laio and M. Parrinello, Free-energy landscape for  $\beta$  hairpin folding from combined parallel tempering and metadynamics, *J. Am. Chem. Soc.*, 2006, **128**(41), 13435–13441.

51 G. Fiorin, A. Pastore, P. Carloni and M. Parrinello, Using metadynamics to understand the mechanism of calmodulin/target recognition at atomic detail, *Biophys. J.*, 2006, **91**(8), 2768–2777.

52 F. Trudu, D. Donadio and M. Parrinello, Freezing of a Lennard-Jones fluid: From nucleation to spinodal regime, *Phys. Rev. Lett.*, 2006, **97**(10), 105701.

53 D. Quigley and P. M. Rodger, Metadynamics simulations of ice nucleation and growth, *J. Chem. Phys.*, 2008, **128**(15), 154518.

54 D. Quigley and P. Mark Rodger, Free energy and structure of calcium carbonate nanoparticles during early stages of crystallization, *J. Chem. Phys.*, 2008, **128**, 221101.

55 P. J. Steinhardt, D. R. Nelson and M. Ronchetti, Icosahedral bond orientational order in supercooled liquids, *Phys. Rev. Lett.*, 1981, **47**(18), 1297.

56 P. J. Steinhardt, D. R. Nelson and M. Ronchetti, Bond-orientational order in liquids and glasses, *Phys. Rev. B: Condens. Matter Mater. Phys.*, 1983, **28**(2), 784.

57 M. Jae Ko, N. Waheed, M. S. Lavine and G. C. Rutledge, Characterization of polyethylene crystallization from an oriented melt by molecular dynamics simulation, *J. Chem. Phys.*, 2004, **121**(6), 2823–2832.

58 N. Waheed, M. J. Ko and G. C. Rutledge, Molecular simulation of crystal growth in long alkanes, *Polymer*, 2005, **46**(20), 8689–8702.

59 E. E. Santiso and B. L. Trout, A general set of order parameters for molecular crystals, *J. Chem. Phys.*, 2011, **134**(6), 064109.

60 A. Barducci, G. Bussi and M. Parrinello, Well-tempered metadynamics: a smoothly converging and tunable free-energy method, *Phys. Rev. Lett.*, 2008, **100**(2), 020603.

61 A. Laio and M. Parrinello, Escaping free-energy minima, *Proc. Natl. Acad. Sci. U. S. A.*, 2002, **99**(20), 12562–12566.

62 A. Barducci, M. Bonomi and M. Parrinello, Metadynamics, *Wiley Interdiscip. Rev.: Comput. Mol. Sci.*, 2011, **1**(5), 826–843.

63 C. Abrams and G. Bussi, Enhanced sampling in molecular dynamics using metadynamics, replica-exchange, and temperature-acceleration, *Entropy*, 2014, **16**(1), 163–199.

64 J. F. Dama, M. Parrinello and G. A. Voth, Well-tempered metadynamics converges asymptotically, *Phys. Rev. Lett.*, 2014, **112**(24), 240602.

65 P. Tiwary and M. Parrinello, A time-independent free energy estimator for metadynamics, *J. Phys. Chem. B*, 2014, **119**(3), 736–742.

66 P. Raiteri, A. Laio, F. Luigi Gervasio, C. Micheletti and M. Parrinello, Efficient reconstruction of complex free energy landscapes by multiple walkers metadynamics, *J. Phys. Chem. B*, 2006, **110**(8), 3533–3539.

67 M. James Abraham, T. Murtola, R. Schulz, S. Páll, J. C. Smith, B. Hess and E. Lindahl, Gromacs: High performance molecular simulations through multi-level parallelism from laptops to supercomputers, *SoftwareX*, 2015, **1**, 19–25.

68 G. A. Tribello, M. Bonomi, D. Branduardi, C. Camilloni and G. Bussi, Plumed 2: New feathers for an old bird, *Comput. Phys. Commun.*, 2014, **185**(2), 604–613.

69 The PLUMED Consortium. Promoting transparency and reproducibility in enhanced molecular simulations. *Nat. Methods*, 16:670–673, 2019. For the full list of researches from the PLUMED Consortium, see <https://www.plumed-nest.org/consortium.html>.

70 G. Bussi, D. Donadio and M. Parrinello, Canonical sampling through velocity rescaling, *J. Chem. Phys.*, 2007, **126**(1), 014101.

71 M. Parrinello and A. Rahman, Polymorphic transitions in single crystals: A new molecular dynamics method, *J. Appl. Phys.*, 1981, **52**(12), 7182–7190.



72 K. Burke, Perspective on density functional theory, *J. Chem. Phys.*, 2012, **136**, 150901.

73 A. D. Becke, Perspective: Fifty years of density-functional theory in chemical physics, *J. Chem. Phys.*, 2014, **140**, 18A301.

74 H. S. Yu, S. L. Li and D. G. Truhlar, Perspective: Kohn-sham density functional theory descending a staircase, *J. Chem. Phys.*, 2016, **145**, 130901.

75 R. J. Maurer, C. Freysoldt, A. M. Reilly, J. G. Brandenburg, O. T. Hofmann, T. Björkman, S. Lebègue and A. Tkatchenko, Advances in density-functional calculations for materials modeling, *Annu. Rev. Mater. Res.*, 2019, **49**(3), 1–3.

76 J. G. Brandenburg, E. Caldeweyher and S. Grimme, Screened exchange hybrid density functional for accurate and efficient structures and interaction energies, *Phys. Chem. Chem. Phys.*, 2016, **18**, 15519–15523.

77 E. Caldeweyher and J. G. Brandenburg, Simplified dft methods for consistent structures and energies of large systems, *J. Phys.: Condens. Matter*, 2018, **30**, 213001.

78 R. Sure and S. Grimme, *Chem. – Eur. J.*, 2017, **23**, 5687–5691.

79 S. Roesel, H. Quanz, C. Logemann, J. Becker, E. Mossou, L. C. Delgado, E. Caldeweyher, S. Grimme and P. R. Schreiner, London dispersion enables the shortest intermolecular hydrocarbon h···h contact, *J. Am. Chem. Soc.*, 2017, **139**, 428–7431.

80 S. Grimme, A. Hansen, J. G. Brandenburg and C. Bannwarth, Dispersion-corrected mean-field electronic structure methods, *Chem. Rev.*, 2016, **116**, 5105–5154.

81 G. J. O. Beran, Modeling polymorphic molecular crystals with electronic structure theory, *Chem. Rev.*, 2016, **116**(9), 5567–5613.

82 J. Klimeš and A. Michaelides, Perspective: Advances and challenges in treating van der Waals dispersion forces in density functional theory, *J. Chem. Phys.*, 2012, **137**, 120901.

83 A. Erba, J. Baima, I. Bush, R. Orlando and R. Dovesi, Large-scale condensed matter dft simulations: Performance and capabilities of the crystal code, *J. Chem. Theory Comput.*, 2017, **13**, 5019–5027.

84 R. Dovesi, A. Erba, R. Orlando, C. M. Zicovich-Wilson, B. Civalleri, L. Maschio, M. Réat, S. Casassa, J. Baima, S. Salustro and B. Kirtman, *Wiley Interdiscip. Rev.: Comput. Mol. Sci.*, 2018, **8**, e1360.

85 R. Sure and S. Grimme, Corrected small basis set Hartree-Fock method for large systems, *J. Comput. Chem.*, 2013, **34**, 1672–1685.

86 M. Cutini, B. Civalleri, M. Corno, R. Orlando, J. G. Brandenburg, L. Maschio and P. Ugliengo, Assessment of different quantum mechanical methods for the prediction of structure and cohesive energy of molecular crystals, *J. Chem. Theory Comput.*, 2016, **12**, 3340–3352.

87 M. Elstner, D. Porezag, G. Jungnickel, J. Elsner, M. Haugk, T. Frauenheim, S. Suhai and G. Seifert, Self-consistent-charge density-functional tight-binding method for simulations of complex materials properties, *Phys. Rev. B: Condens. Matter Mater. Phys.*, 1998, **58**(11), 7260–7268.

88 B. Aradi, B. Hourahine and T. Frauenheim, Dftb+, a sparse matrix-based implementation of the dftb method, *J. Phys. Chem. A*, 2007, **111**(26), 5678–5684.

89 J. G. Brandenburg and S. Grimme, Accurate Modeling of Organic Molecular Crystals by Dispersion-Corrected Density Functional Tight Binding (DFTB), *J. Phys. Chem. Lett.*, 2014, **5**, 1785–1789.

90 J. G. Brandenburg, J. Potticary, H. A. Sparkes, S. L. Price and S. R. Hall, Thermal expansion of carbamazepine: Systematic crystallographic measurements challenge quantum chemical calculations, *J. Phys. Chem. Lett.*, 2017, **8**, 4319–4324.

